A Nowcasting Approach for Low-Earth-Orbiting Hyperspectral Infrared Soundings within the Convective Environment

BRIAN H. KAHN,[a] EMILY B. BERNDT,[b,c] JONATHAN L. CASE,[d] PETER M. KALMUS,[a] AND MARK T. RICHARDSON[a]

[a] *Jet Propulsion Laboratory, California Institute of Technology, Pasadena, California*
[b] *Earth Science Branch, NASA Marshall Space Flight Center, Huntsville, Alabama*
[c] *NASA Short-term Prediction Research and Transition (SPoRT) Center, Huntsville, Alabama*
[d] *ENSCO, Inc., Huntsville, Alabama*

ABSTRACT: Low-Earth-orbiting (LEO) hyperspectral infrared (IR) sounders have significant yet untapped potential for characterizing thermodynamic environments of convective initiation and ongoing convection. While LEO soundings are of value to weather forecasters, the temporal resolution needed to resolve the rapidly evolving thermodynamics of the convective environment is limited. We have developed a novel nowcasting methodology to extend snapshots of LEO soundings forward in time up to 6 h to create a product available within National Weather Service systems for user assessment. Our methodology is based on parcel forward-trajectory calculations from the satellite-observing time to generate future soundings of temperature (T) and specific humidity (q) at regularly gridded intervals in space and time. The soundings are based on NOAA-Unique Combined Atmospheric Processing System (NUCAPS) retrievals from the *Suomi National Polar-Orbiting Partnership* (*Suomi NPP*) and *NOAA-20* satellite platforms. The tendencies of derived convective available potential energy (CAPE) and convective inhibition (CIN) are evaluated against gridded, hourly accumulated rainfall obtained from the Multi-Radar Multi-Sensor (MRMS) observations for 24 hand-selected cases over the contiguous United States. Areas with forecast increases in CAPE (reduced CIN) are shown to be associated with areas of precipitation. The increases in CAPE and decreases in CIN are largest for areas that have the heaviest precipitation and are statistically significant compared to areas without precipitation. These results imply that adiabatic parcel advection of LEO satellite sounding snapshots forward in time are capable of identifying convective initiation over an expanded temporal scale compared to soundings used only during the LEO satellite overpass time.

SIGNIFICANCE STATEMENT: Advection of low-Earth-orbiting (LEO) satellite observations of temperature and specific humidity forward in time exhibits skill in determining where and when convection eventually initiates. This approach provides a foundation for a new nowcasting methodology leveraging thermodynamic soundings derived from hyperspectral infrared (IR) sounders on LEO satellite platforms. This method may be useful for creating time-resolved soundings with the constellation of LEO satellites until hyperspectral infrared soundings are widely available from geostationary platforms.

KEYWORDS: North America; Convective storms/systems; Stability; Storm environments; Satellite observations; Nowcasting

---

1. Introduction

Hyperspectral infrared (IR) sounders have significant yet untapped potential to monitor the preconvective environment and convective storm life cycle. This potential was previously demonstrated with surface-based upward-looking Atmospheric Emitted Radiance Interferometer (AERI) (e.g., Feltz and Mecikalski 2002; Wagner et al. 2008) and space-based IR sounders in low-Earth-orbiting (LEO) satellites (e.g., Botes et al. 2012; Jones and Stensrud 2012; Weisz et al. 2015; Gartzke et al. 2017; Kalmus et al. 2019; Smith et al. 2020). The Atmospheric Infrared Sounder (AIRS) on the Earth Observing System (EOS) *Aqua* satellite (Chahine et al. 2006), the Cross-track Infrared Sounder (CrIS) on *Suomi National Polar-Orbiting Partnership* (*Suomi NPP*) and *NOAA-20* (Han et al. 2013), and the Infrared Atmospheric Sounding Interferometer (IASI) on the

European Space Agency (ESA) MetOp satellite series (Blumstein et al. 2004) are presently operating in LEO and provide vertical profiles of temperature (T) and specific humidity (q) in clear and partly cloudy scenes. Continuous swaths between 1650 and 2200 km wide provide soundings of T and q at approximately 0130 and 1330 LT from *Aqua*, *Suomi NPP*, and *NOAA-20*, and 0930 and 2130 LT from MetOp satellite platforms. While the temporal snapshots have proven to be valuable for operational weather forecasting (Berndt et al. 2016; Weaver et al. 2019; Esmaili et al. 2020; Berndt et al. 2020; Kalluri et al. 2022), they are unable to resolve rapid temporal changes in the convective environment of a few hours or less. The one exception is the intermittent and irregularly spaced time differences and overlapping regions of limited swath width between *Aqua*, *Suomi NPP*, and *NOAA-20* at approximately 0130 and 1330 LT.

A global ring of hyperspectral IR sounders in geostationary (GEO) orbit could eventually eliminate the temporal observing gap outside of the polar regions (Schmit et al. 2009). The

---

Geostationary Interferometric Infrared Sounder (GIIRS) on *Fengyun 4* (*FY-4*) (Yang et al. 2017) is the first hyperspectral IR sounder in GEO, and the Infrared Sounder (IRS) on MeteoSat Third Generation-Sounder (MTG-S) (Holmlund et al. 2021) is planned for launch in the mid-2020s. GEO sounding data will also be an important component of future operational numerical weather prediction (NWP) data assimilation systems (e.g., Burrows 2019). GIIRS radiances in water vapor channels were used in data assimilation and improved the timing, location, and amount of rainfall in convective events (Yin et al. 2021, 2022). The potential added value of GEO over currently available LEO Level 1 (L1) radiances or Level 2 (L2) thermodynamic profiles is quantified using observing system simulation experiments (OSSEs) (Hoffman and Atlas 2016); however, these experiments remain in their early stages (e.g., Li et al. 2018; Adkins et al. 2021; Wang et al. 2021). Nevertheless, LEO hyperspectral IR radiances or derived L2 soundings have a demonstrably positive impact on NWP skill in the convective environment. Jones and Stensrud (2012) showed that AIRS thermodynamic soundings improved mesoscale simulations of moisture variability, convective initiation, and the realism of convective features up to 4 h in advance, even at spatial scales much finer than the AIRS soundings.

The current fleet of LEO hyperspectral IR sounders takes daily observations for a given surface location. The time separation is, however, variable and limited to three or four daily observations at ~0930 and 2130 LT and ~0130 and 1330 LT (Weisz et al. 2015). Two distinct algorithm methodologies exhibit skill in increasing the time resolution of LEO soundings. The first approach combines the high spectral resolution from LEO with the high time resolution of GEO imagery leveraging data fusion (Weisz and Menzel 2019) or data assimilation (Smith et al. 2020) methods. The second approach combines LEO soundings with parcel trajectory modeling to create time-resolved soundings before or after a given LEO overpass (Kalmus et al. 2019, henceforth K19). The trajectory model approach is driven by NWP wind fields that treat individual sounding layers as distinct air parcels that are conserved along moist or dry adiabats. The parcels are then recombined into vertical profiles before or after the satellite overpass time using backward or forward trajectories, respectively. The K19 method was developed with Atmospheric Infrared Sounder (AIRS) version 6 retrievals of T and q (Chahine et al. 2006) to create proximity soundings near reports of tornadoes, large hail, and strong winds after the 1330 UTC *Aqua* overpass over the contiguous United States (CONUS).

K19 showed that convective available potential energy (CAPE) and convective inhibition (CIN) derived from AIRS proximity soundings depend on various severe weather types, including tornado EF scale, hail diameter, and wind speed. Statistically significant separation among a subset of hail, wind, and tornado intensities was demonstrated for lifting condensation level (LCL), level of free convection (LFC), and the maximum value of q within an AIRS profile. While increases in CAPE and decreases in CIN correlated to increasing wind speeds, larger hail size, and stronger tornadoes as

demonstrated previously (e.g., Rasmussen and Blanchard 1998; Doswell and Evans 2003; Thompson et al. 2003; Parker 2014), the K19 correlations were not statistically significant. Given that a vast majority of CONUS thunderstorms do not produce damaging winds, large hail, and/or tornadoes, evaluating CAPE and CIN using proxies for the initiation, location, and intensity of nonsevere convection, such as the timing and total accumulation of precipitation, is warranted.

The K19 approach has similarities to the NearCast model that was designed for operational convective forecasting using GOES-R temperature and moisture soundings (Gravelle et al. 2016). The NearCast model uses Lagrangian parcel trajectories to project equivalent potential temperature and layer precipitable water forward in time (Petersen and Aune 2007). As hyperspectral IR soundings were not available on GOES-R, the approach was tested with soundings derived from the Advanced Baseline Imager (ABI) that provides relatively high horizontal resolution (~10 km) yet vertically coarse resolution. In the case of LEO hyperspectral IR soundings have coarser horizontal resolution (~40 km at nadir view) but with finer vertical resolution. There are trade-offs between horizontal and vertical sounding resolution, and the appropriate trade-off choice depends on the spatial and temporal gradients that are observed in the context of convective initiation.

This investigation was motivated by two thrusts. 1) We have extended the methodology of K19 to full swaths of LEO soundings, adding time resolution after a single, temporally fixed LEO snapshot. 2) We have evaluated these "trajectory-enhanced" swaths of LEO soundings in the context of convective initiation using observed precipitation accumulation as a proxy. This expands beyond usual proximity sounding assessments that solely emphasize severe convective storms.

We will briefly summarize the methodology of K19 with modifications to it that provide spatially and temporally uniform coverage of T and q for near real-time operational weather forecasting applications. The trajectory-based methodology may offer a viable option to fill temporal gaps in satellite-based IR sounding observations within the preconvective environment. The approach described herein is specifically tailored to nowcasting in an operational environment (WMO 2017), between 5 and 7 h after the LEO satellite overpass. A total of 24 cases are examined, covering areas that were hand-selected following criteria that they were nonprecipitating during satellite overpasses, but later developed precipitation. We show that the trajectory-enhanced product has differences in CAPE and CIN between scenes that remain dry and contain measurable precipitation in the one to 6-h nowcasting time frame. These differences are statistically significant in most cases investigated. The relationships between CAPE or CIN and precipitation are weaker and less frequently significant when using the original NUCAPS soundings from overpass time.

The data sources are listed in section 2. The methodology that builds upon K19 is described in section 3. Section 4 details how the 24 hand-selected cases were chosen. Section 5 compares derived convective parameters with rainfall data. In section 6, we discuss potential future research directions.

2. Data

a. NUCAPS

The NOAA-Unique Combined Atmospheric Processing System (NUCAPS; Barnet et al. 2021) provides vertically resolved T and q soundings, surface temperature (T_{sfc}), surface emissivity, cloud top temperature (T_{cld}), effective cloud fraction (ECF), and several species of trace gasses from *Suomi NPP*, *NOAA-20*, and the MetOp satellite series in near–real time. The NUCAPS geophysical retrievals utilize a cloud-clearing approach containing a 3×3 array of Cross-track Infrared Sounder (CrIS) fields of view (FOV) collocated to Advanced Technology Microwave Sounder (ATMS) FOVs within a field of regard (FOR). The nadir-view spatial resolution is approximately 40 km with coarser resolution at higher scan angles. The T and q values are reported at 100 separate pressure levels between 1100 and 0.016 hPa. The effective vertical resolution of T and q is ~2–3 km despite finer vertical gridding as the information content is smoothed vertically (Maddy and Barnet 2008; Smith and Barnet 2020). Each sounding profile has a quality control (QC) label of "*best*," "*good*," or "*do not use*." Only *best* and *good* soundings are selected for this investigation. *Best* soundings are characterized by successful IR and microwave (MW) retrievals, *good* represents where the IR sounding has failed but the MW retrieval was successful, and soundings are assigned *do not use* when both the IR and MW retrievals failed.

Comparisons of NUCAPS soundings against high-quality radiosondes show that profiles of T have biases within ±1 K and root-mean-square (RMS) differences of 0.5–1.5 K, with higher RMS differences as altitude increases. Profiles of q have biases of ±20% and RMS values of 10%–30% (e.g., Nalli et al. 2013, 2018). The bias and RMS estimates for NUCAPS closely resemble previous investigations into the performance of AIRS Team sounder retrievals (e.g., Chahine et al. 2006; Divakarla et al. 2006; Tobin et al. 2006; Wong et al. 2015).

The interpretation of bias and RMS estimates from differences between satellite soundings and radiosondes are inherently limited by (i) pervasive T and q variability at spatial scales of 50 km or less, (ii) temporal mismatches at hourly or subhourly time scales, (iii) geometrical differences in the sampling space among radiosondes and the satellite viewing line of sight, and (iv) the presence of clouds. Bias and RMS estimates will therefore never be zero because of the vastly different observation techniques. Sun et al. (2017) showed that RMS differences of both T and q increase by a factor of 2 as time mismatches of coincident NUCAPS and radiosonde matchups increase from 1 to 6 h. Iturbide-Sanchez et al. (2018) demonstrated that NUCAPS T and dewpoint (T_d) exhibit relatively small biases (from −1.6 to 1.7 K) and standard deviations (from +2.6 to 3.7 K) within 100 hPa of the surface when compared to radiosondes. To summarize, NUCAPS satellite soundings faithfully capture the magnitudes and variability of T and q in the mesoscale range despite the reduced vertical resolution with respect to radiosondes.

b. GDAS/GFS

The Global Forecast System (GFS)/Global Data Assimilation System (GDAS) variational analysis and NWP model was developed by the National Centers for Environmental Prediction (NCEP) (Wang et al. 2013). The 3D wind profiles are available every 3 h on a 0.25° × 0.25° grid and are used to calculate parcel trajectories obtained from NOAA's Hybrid Single-Particle Lagrangian Integrated Trajectory model (HYSPLIT; Stein et al. 2015), described in section 3.

c. MRMS

The K19 approach applies to the vast majority of nonsevere convective storms. Accumulated precipitation is thus an appropriate proxy that reflects the hydrological aspects of precipitating convection and the timing and location of convective initiation. Developed by the National Severe Storms Laboratory (NSSL), the hourly Multi-Radar Multi-Sensor (MRMS) quantitative precipitation estimate (QPE) blends ground-based radar and rain gauge observations into an optimal estimate of precipitation (Zhang et al. 2016). The GaugeCorrQPE01H field contains 1-h precipitation estimates at a horizontal resolution of 0.01° in latitude and longitude. GaugeCorrQPE01H is averaged to 0.5° × 0.5° resolution including nonprecipitating data points.

3. NUCAPS-FCST

The soundings calculated later than the LEO observing time are termed "NUCAPS Forecast" (NUCAPS-FCST) and build upon the methods of K19. In our investigation, swaths from *Suomi NPP* and *NOAA-20* are combined into a larger swath to maximize spatial coverage and density of soundings. With access to low-latency LEO observations through direct broadcast, and adequate computational resources that expeditiously calculate air parcel trajectories, NUCAPS-FCST is usable in a quasi-operational forecasting test bed framework within a few hours or less of the satellite overpass time (Esmaili et al. 2020).

a. Changes from K19

K19 identified atmospheric columns where severe convective events occurred and then back-traced the constituent parcels onto earlier AIRS retrieval locations. This paper instead takes NUCAPS retrievals and projects parcel trajectories forward in time. Every level with $P > 100$ hPa within each sounding FOR is treated as a point measurement centered on a corresponding air parcel. The parcels are assigned new altitudes, latitudes, and longitudes consistent with their respective calculated air parcel trajectories obtained from HYSPLIT driven by GFS forecast inputs. A list of changes from K19 are found in Table 1.

The zeroth "overpass" time step includes all footprints within 1800–1959 UTC and is assigned a 1900 UTC analysis time. To ensure that all footprints are included in all time steps, the first FCST time step is 2000 UTC, and the time steps then proceed hourly through 0100 UTC of the next day. At each hour the mean T and q of all parcels within each grid

TABLE 1. List of characteristics that differ between K19 and the present study.

K19	Present study
Trajectories backward in time from NCEI Storm Event locations that occurred after satellite swath	Trajectories forward in time from the satellite swath up to 6 h into the future
Aqua AIRS V6 soundings	*Suomi NPP* and *NOAA-20* NUCAPS soundings
No spatial gridding	0.5° × 0.5° grids
Statistical examination between tornado EF scale, hail diameter, wind speed	Statistical examination between no precipitation vs light or heavy precipitation observed by MRMS
Offline research product	Quasi-operational product tested in AWIPS II
32-km, 3-h NARR and 12-km, 1-h NAM winds	0.25° GDAS/GFS winds
40 levels backtraced from Storm Events between the surface and 100 hPa	All sounding levels forward traced between the surface and 60 hPa, averaged into 80-hPa bins
Examined NCEI Storm Events between 2003 and 2016	Examined 24 hand-selected cases between March and July 2020

box are calculated for an output grid of 0.5° × 0.5° in latitude–longitude and a vertical resolution of 80 hPa. The regridded profiles are not constrained to follow the original NUCAPS pressure levels as parcels may rise or descend. Each regridded NUCAPS-FCST sounding may be composed of different numbers of parcels according to the trajectories calculated by HYSPLIT.

Restricting NUCAPS-FCST to best and good QC increases the fidelity of the forecast soundings and derived convective parameters. Adding the do not use QC soundings increases the frequency of vertically spurious structures in the forecast soundings and discontinuities in the derived convective parameters (not shown). Similarly, restricting NUCAPS-FCST to best QC only is detrimental as soundings are limited to the clearest skies, eliminating some of the T and q gradients that are critical for convective initiation (not shown).

The air parcel T is adjusted at each time step along dry or moist adiabats as appropriate using the SHARPpy 1.4.0 package
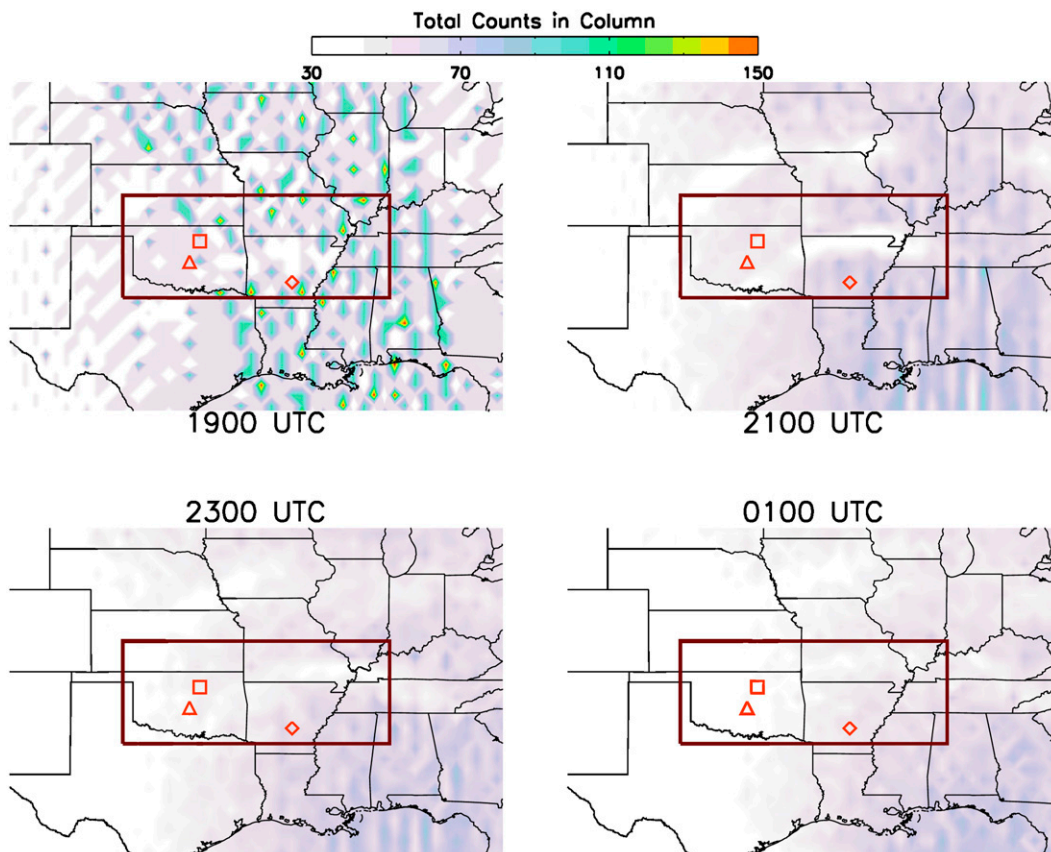

FIG. 1. Total counts in the atmospheric column using 0.5° × 0.5° gridding at 1900, 2100, and 2300 UTC 27 Mar 2020 and 0100 UTC 28 Mar 2020. The total counts include the number of air parcels within each grid box in the vertical column from the surface to 100 hPa. The rectangular box depicts a region of further analysis summarized in Table 2.
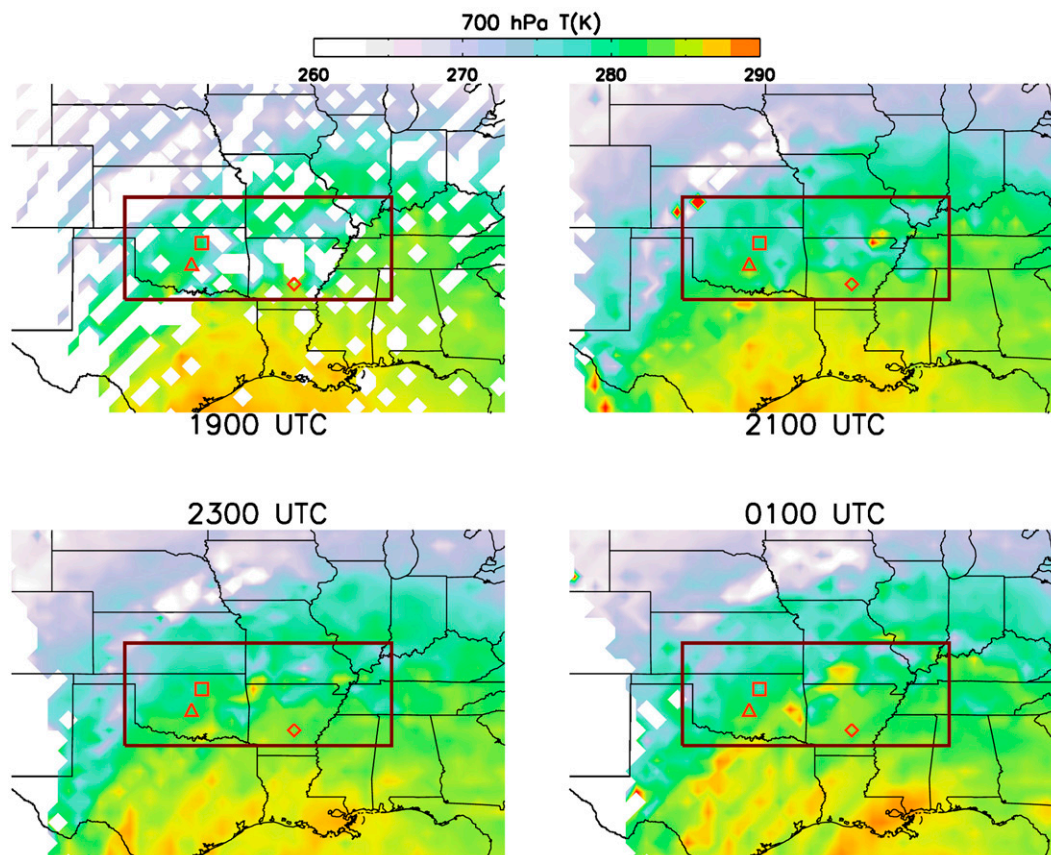
FIG. 2. Vertically interpolated *T* (K) at 700 hPa at 1900, 2100, and 2300 UTC 27 Mar 2020, and 0100 UTC 28 Mar 2020. Red symbols depict three locations of vertical soundings shown in Fig. 4.

(Blumberg et al. 2017). Any parcel advected below Earth's surface (estimated by NUCAPS surface pressure) is removed. The application of adiabatic parcel theory is expected to perform best in nonprecipitating preconvective environments that are generally clear or partly cloudy. NUCAPS excels in these conditions that are frequent in CONUS during warm season preconvective environments.

b. Adapting to operations

NUCAPS-FCST is intended for operational forecasting applications where rapid production turnaround is necessary to be useful to forecasters (Esmaili et al. 2020). While observations or NWP simulations of T_{sfc} and T_d could supplement missing and/or poor-quality data with near surface values to create a more robust structure within the PBL (Gartzke et al. 2017; Bloch et al. 2019), this enhancement is not available for this version of NUCAPS-FCST. The merging of observations and NWP simulations is potentially promising but fraught with pitfalls such as discontinuities that vary between NWP models, and among different runs for the same model. Blending observations and NWP simulations is beyond the scope of this investigation.

The NASA Short-term Prediction Research and Transition (SPoRT) Center has an established history of transitioning NASA satellite observations and capabilities to end users within the context of a research-to-operations/operations-to-research paradigm (Jedlovec 2013). Real-time processing of NUCAPS-FCST was developed and managed by SPoRT in support of NOAA's Hazardous Weather Testbed (HWT; Calhoun et al. 2021) activities during spring 2019, and was reinstated during spring and summer 2020 despite the cancellation of HWT as a result of the coronavirus pandemic. A detailed description of our approach to operationalizing NUCAPS-FCST is included in appendix A.

c. 27 March 2020 case study

Some typical outputs (e.g., parcel counts, *T*, *q*, MUCAPE, MUCIN) are illustrated for 27 March 2020, a case that is typical for those that exhibit differences in convective parameters between precipitating and nonprecipitating scenes. Figure 1 shows how sampling gaps at overpass time are gradually filled in as parcels advect, and also shows that areas of convergence (divergence) will have more (fewer) number of parcels as time advances. Additionally, the parcel counts in each grid box provides a sense of the amount of information content available at each location which could increase or decrease confidence in the integrity of the derived fields.
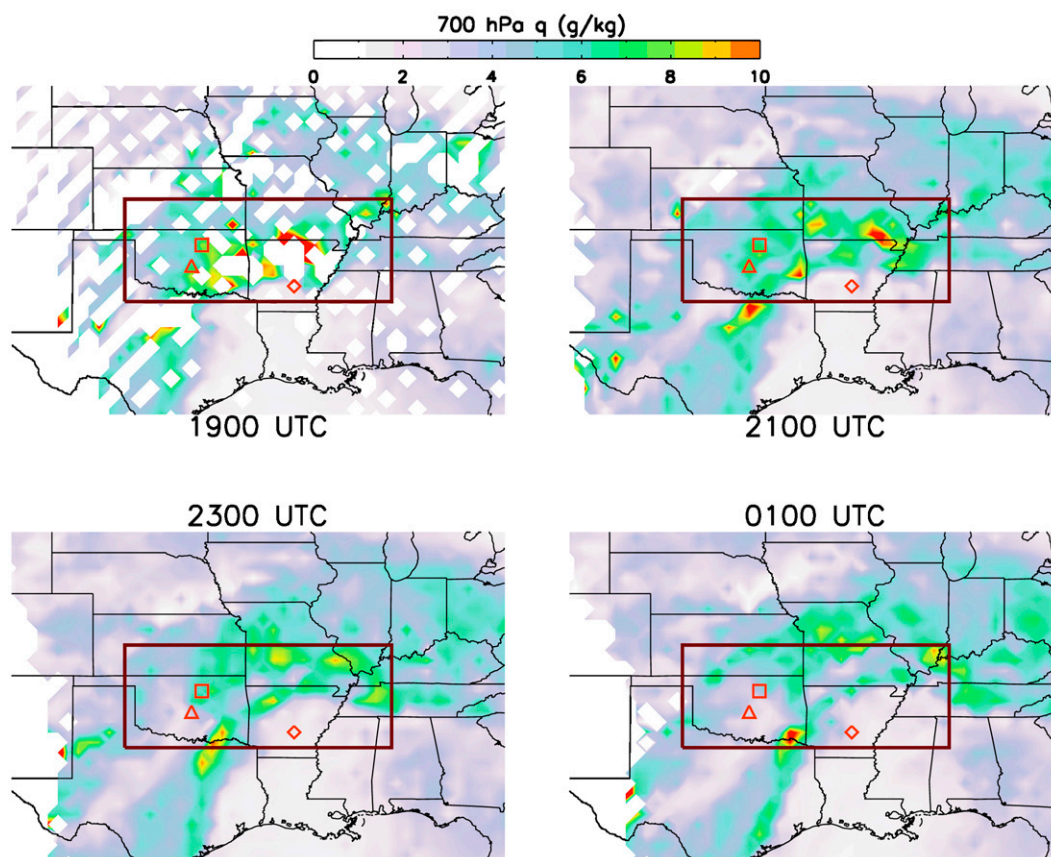
FIG. 3. Vertically interpolated q (g kg^{-1}) at 700 hPa at 1900, 2100, and 2300 UTC 27 Mar 2020 and 0100 UTC 28 Mar 2020.

Three-dimensional NUCAPS-FCST fields of T (Fig. 2) and q (Fig. 3) are interpolated to the 700-hPa level at 1900, 2100, and 2300 UTC 27 March 2020, and 0100 UTC 28 March 2020. Jones and Stensrud (2012) showed that midtropospheric levels in AIRS retrievals are highly impactful for convective storm forecasting. Therefore, the 700-hPa level is used to help illustrate the case study. The white areas are consistent with grid boxes containing zero counts that are common at higher swath satellite viewing zenith angles where the sounding resolution is coarser than $0.5° \times 0.5°$, or areas with large cloud fractions that frequently have poor quality soundings. Regions with notable horizontal T and q gradients are consistent with a stationary front extending from southeast Colorado, through northern Oklahoma, into central Missouri, with a dryline oriented north–south over west Texas (not shown). While the thermodynamic fields are generally coherent and realistic, a few outliers (e.g., west Kansas at 2100 UTC in Fig. 2) are attributable to low parcel counts.

Selected NUCAPS-FCST T and q profiles (Fig. 4) exhibit vertical structures consistent with this case's mesoscale pattern and time evolution. Note the significant midtropospheric drying in the three sets of soundings. The two sets of soundings over Oklahoma show drying in the wake of the eastward trajectory of convective storms. In contrast, the drying in the

soundings over Arkansas is consistent with the strong convective cap in place over this period. Lower tropospheric stabilization is observed in the northern Oklahoma soundings. Convective indices are calculated from regridded T and q soundings assuming the most unstable (MU) parcels with the SHARPpy Python package. The values of CAPE and CIN are reported for each sounding profile in Fig. 4. The soundings over Arkansas reflect higher values of CIN where it remained free of convective storms. Over Oklahoma, convective storms occurred earlier in the time period before midtropospheric drying and lower tropospheric stabilization settled in behind the storms. A limited set of radiosonde comparisons of T and q are described in appendix B.

CAPE is shown in Fig. 5 with an overlay of MRMS 1-h rainfall accumulation to depict the occurrence of convection. Severe and nonsevere convective storms were prevalent throughout CONUS on this day (not shown). Areas of missing CAPE at 1900 UTC align with the sampling limitations previously discussed (Fig. 1). The heavy precipitation in the MRMS at 0100 UTC falls in an area of a high horizontal gradient in CAPE. Corresponding CIN is shown in Fig. 6 for the same area and period as depicted in Fig. 5. Weak CIN prevails in regions where rainfall occurs, while much larger values of CIN are found throughout the southern part of CONUS where no
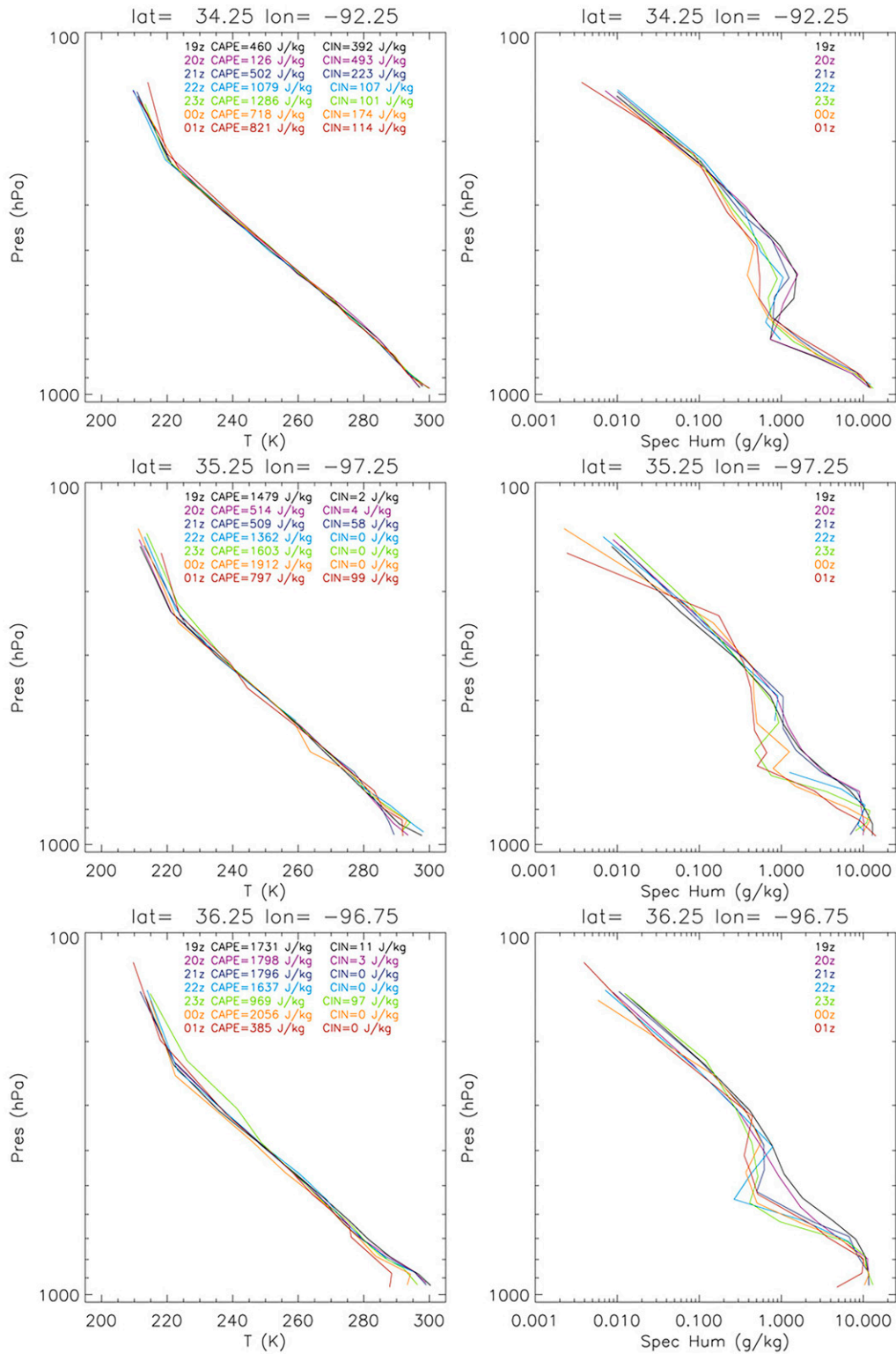
FIG. 4. Vertical profiles of T and q for the (top) diamonds, (middle) triangles and (bottom) squares shown in Figs. 1–3. Hourly soundings are shown (NUCAPS-FCST) from 1900 UTC 27 Mar 2020 to 0100 UTC 28 Mar 2020. The vertical binning is performed in 80-hPa layers.
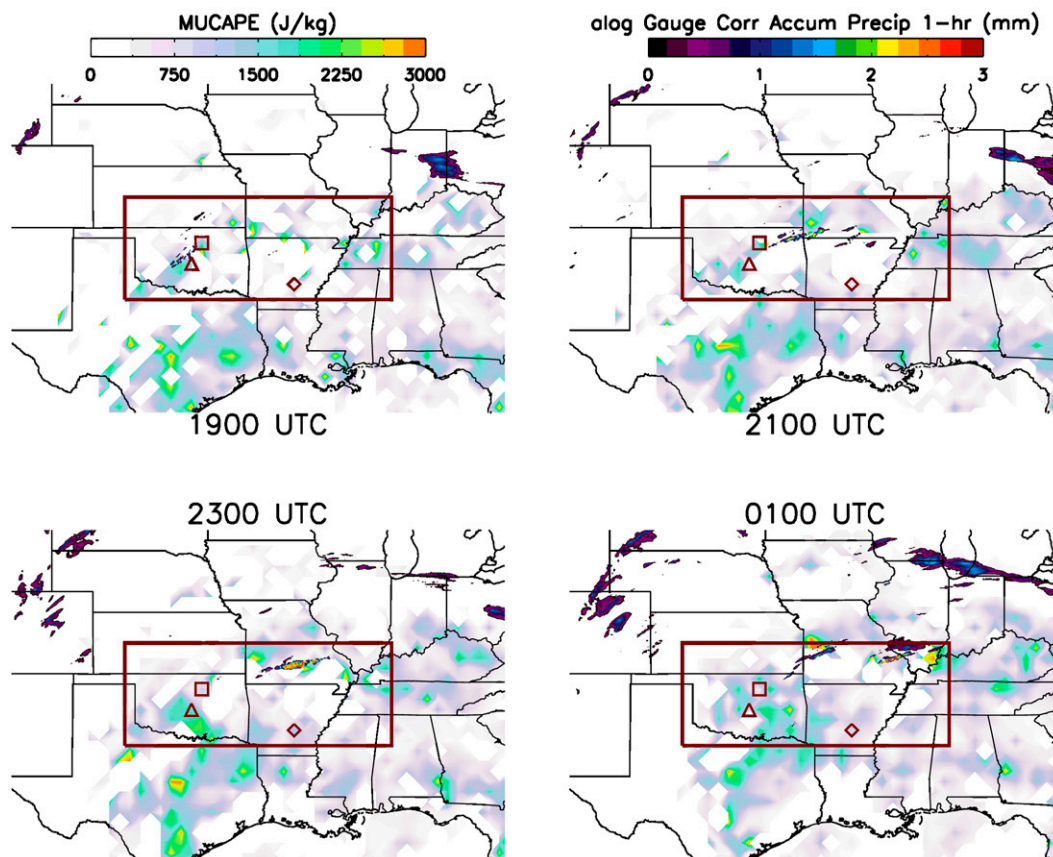
FIG. 5. MUCAPE with MRMS 1-h natural log QPE overlay at 1900, 2100, and 2300 UTC 27 Mar 2020 and 0100 UTC 28 Mar 2020.

rainfall is observed. Upon examination of the 27 March 2020 case, the magnitudes, spatial gradients, and temporal changes in NUCAPS-FCST CAPE and CIN are approximately consistent with the timing and location of convective rainfall occurrence.

4. Two hypotheses and selection of cases

As outlined in the 27 March 2020 example above, the observational target is the timing and location of convective initiation as evidenced by MRMS rainfall. Cold pools, stable layers, extensive cloud cover, subgrid convection, and other phenomena associated with rainfall before 1900 UTC may complicate the interpretation of convective initiation after 1900 UTC. Therefore, the focus is on areas of CONUS at 1900 UTC that have minimal occurrences of these complicating factors. We posit that NUCAPS-FCST adds value through (i) depicting horizontal gradients in CAPE and CIN, and (ii) resolving temporal changes of CAPE and CIN in the hours after the satellite observations. Following (i), our first hypothesis is that *increased values of CAPE, and decreased values of CIN over scales of a few hundred kilometers or less, indicate increased likelihood of convective initiation*. Following (ii), our second hypothesis is that *CAPE and CIN analyses at 1900 UTC are less likely to predict convective initiation after 1900 UTC than CAPE and CIN fields estimated at later times from the HYSPLIT forward trajectories*.

Testing the two convective initiation-centric hypotheses requires selection of regions relatively devoid of precipitation at 1900 UTC. The larger the area considered, the more likely it is that thick clouds or precipitation impact retrieval quality such that more *do not use* QC retrievals are encountered. The smaller the area considered, the smaller the sample size and reduced statistical power of any analysis. Furthermore, smaller areas increase the likelihood that parcel trajectories may move into an area of interest from a region with the aforementioned complicating factors. Spatially extensive areas with concurrent high values of CIN and CAPE without convective initiation during the 6-h time period are avoided. Gridded MRMS rainfall data provide a means to identify areas where convection initiated after 1900 UTC. This approach is generally consistent with the size of the latitude–longitude box considered in the 27 March 2020 case study. A total of 24 cases are listed in Table 2. The cases each capture a fairly quiescent preconvective environment that evolves into a region of active convection, with a minimum of complicating factors. These cases were taken from 1 March 2020 to 31 July 2020, spanning a variety of convective scenarios, with a wide range of mean MUCAPE and MUCIN values (Table 2). The $0.01° \times 0.01°$ MRMS
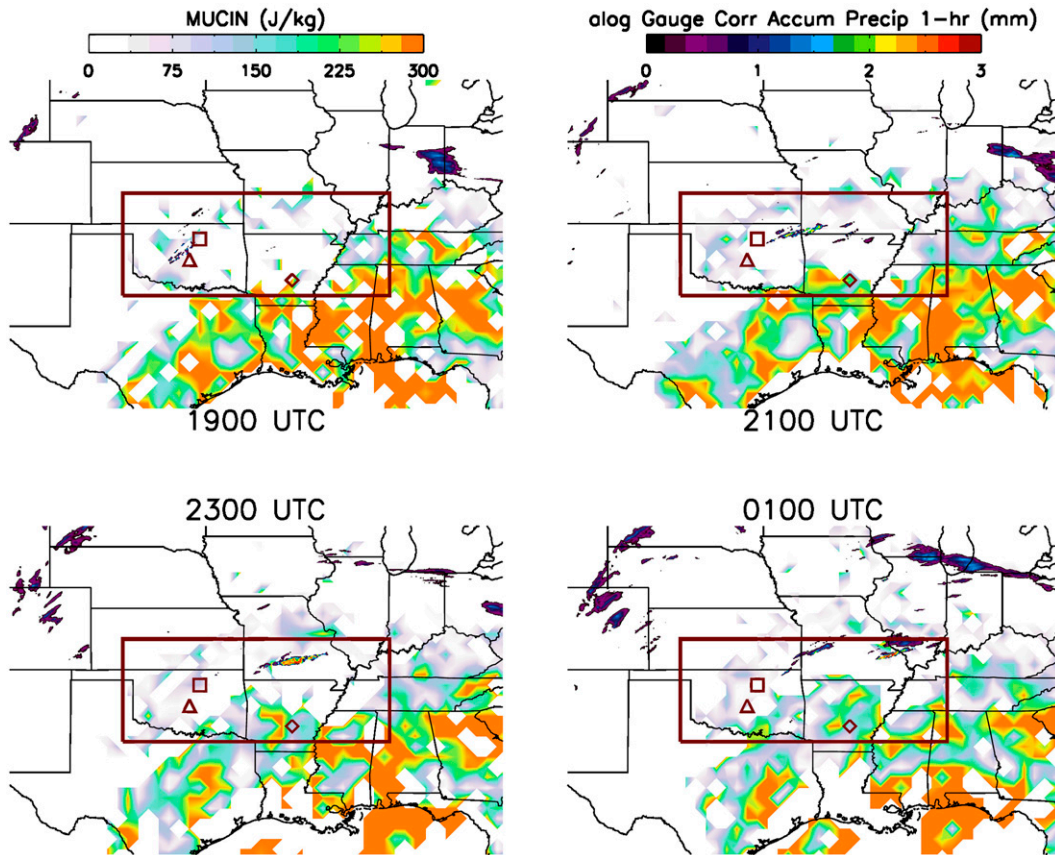
FIG. 6. MUCIN with MRMS 1-h natural log QPE overlay at 1900, 2100, and 2300 UTC 27 Mar 2020 and 0100 UTC 28 Mar 2020.

GaugeCorrQPE01H data (including zero values) are averaged within the same $0.5° \times 0.5°$ NUCAPS-FCST grid box. Hourly CAPE and CIN are matched in space and time to hourly MRMS rainfall within the 0–6-h NUCAPS-FCST time period. A $0.5° \times 0.5°$ gridbox-averaged accumulation greater than 0 mm and ≤ 1 mm is regarded as *light* precipitation, while an accumulation > 1 mm is regarded as *heavy* precipitation. Accumulations of 0 mm are labeled *no precipitation*.

Despite the caveats regarding diabatic processes that operate on air parcel evolution, NUCAPS-FCST should capture many of the mesoscale changes in the vertical and horizontal structure of T and q that contribute to the evolution of CAPE and CIN after the satellite overpasses. This is supported by initial forecaster feedback during the 2019 HWT that suggests NUCAPS-FCST can indicate regions that undergo convective initiation when analyzing patterns of CAPE and CIN that qualitatively compared well to trusted model output.

5. Results

a. Individual cases

A two-sample Student's t test assuming unequal sample sizes but similar variances is used to test our two hypotheses. The equations are now framed with respect to the first hypothesis:

$$t = \frac{\bar{x} - \bar{y}}{s_p \sqrt{\dfrac{1}{m} + \dfrac{1}{n}}}, \tag{1}$$

where t is the t statistic, x is for CAPE values with no precipitation, y is for CAPE values with either (i) light or (ii) heavy precipitation according to MRMS, m is the sample size for x, and n is the sample size for y. There are two different tests performed for CAPE: one that examines the differences in CAPE with no precipitation against CAPE with light precipitation, and a second that examines CAPE with no precipitation against CAPE with heavy precipitation. The same procedure is then independently followed for values of CIN. The pooled standard deviation s_p is defined as follows:

$$s_p = \sqrt{\frac{(m-1)s_x^2 + (n-1)s_y^2}{m+n-2}}. \tag{2}$$

The statistical significance for the 24 cases is calculated individually and is indicated as bold font in Table 2 with respect to the first hypothesis. The entire 0–6-h nowcasting time frame is used together in the t test.

TABLE 2. Twenty-four hand-selected cases during 2020 according to the desired criterion. Dates, latitude–longitude bounding box, and CAPE/CIN (J kg^{-1}) for scenes with no precipitation, light precipitation ($\leq$1 mm), and heavy precipitation (>1 mm) averaged over the 0.5° × 0.5° grid box for all MRMS grid points (raining and nonraining). The bold values indicate statistically significant differences between "no precip" and "light precip," and "no precip" and "heavy precip," which are consistent with the first hypothesis (higher CAPE and lower CIN). The bold italicized values indicate statistically significant differences that are contrary to the first hypothesis. All values are 6-h averages within the specified domain with CAPE and CIN values filtered by MRMS rainfall estimates at 0.5° × 0.5° resolution for each hour within the 6-h time period.

Case No.	Date	Lat range (°N)	Lon range (°W)	CAPE no precip	CAPE light precip	CAPE heavy precip	CIN no precip	CIN light precip	CIN heavy precip
1	1 Mar	32–40	95–85	160	**236**	**544**	65	**46**	28
2	2 Mar	36–40	95–85	367	293	**526**	38	40	38
3	3 Mar	36–42	85–78	104	**125**	139	97	**53**	**38**
4	12 Mar	32–38	100–89	293	320	**405**	64	**61**	**41**
5	20 Mar	32–38	100–80	242	**464**	**539**	145	**47**	**15**
6	24 Mar	32–35	95–85	242	**391**	**466**	47	**44**	**11**
7	27 Mar	34–38	100–88	686	**848**	**1187**	111	**77**	**60**
8	2 Apr	34–39	96–90	266	305	**276**	75	65	**21**
9	4 Apr	36–40	94–88	117	71	—	84	142	—
10	5 Apr	34–38	85–75	196	**290**	189	38	**22**	8
11	7 Apr	40–44	93–83	425	385	**518**	79	74	**43**
12	9 Apr	38–42	90–80	83	**156**	**313**	271	**110**	—
13	13 Apr	42–46	96–84	139	**214**	—	135	**85**	—
14	22 Apr	40–44	100–90	325	*259*	443	37	**29**	**16**
15	28 Apr	34–38	100–90	676	**1099**	**1156**	88	63	**55**
16	4 May	34–38	100–90	526	576	**806**	166	**57**	**41**
17	5 May	28–32	100–90	555	576	426	111	94	148
18	14 May	34–40	100–90	582	588	**580**	74	**61**	**71**
19	16 May	36–40	87–77	437	366	435	46	**27**	**21**
20	17 May	24–30	85–80	382	**678**	**730**	75	**30**	**29**
21	26 May	28–34	97–90	516	524	**665**	55	60	**47**
22	14 Jul	40–44	100–90	501	327	369	133	**98**	**39**
23	19 Jul	36–40	100–90	660	758	**817**	106	91	**86**
24	28 Jul	36–40	100–90	219	**256**	**282**	91	**69**	**69**

For light precipitation, 10 out of 24 cases have significantly higher values of CAPE and only one case has significantly lower CAPE (22 April 2020) than "no precipitation" grid boxes. A total of 8 out of 13 of the remaining cases have insignificantly higher values of CAPE for light precipitation. For heavy precipitation, 15 out of 24 cases have significantly higher CAPE. Of the remaining nine cases, two incidentally did not include any 0.5° × 0.5° scenes with heavy precipitation, while seven cases exhibited a mixture of insignificantly higher and lower values of CAPE. More cases exhibit significant CAPE enhancements for the heavier precipitating scenes compared to light precipitating scenes, which is expected as additional enhancement of CAPE is indicative of stronger convective potential and subsequent precipitation rates.

Concerning CIN, for light precipitation, 15 out of 24 cases have significantly lower values. Six of the remaining nine insignificant differences also show a reduction in CIN for light precipitation. For areas of heavy precipitation, 17 out of 24 cases have significantly lower values of CIN. Four cases are a mixed bag, while three cases do not have any observations of heavy precipitation (i.e., no values in Table 2. Note that some grid cells return valid CAPE but invalid CIN). As with CAPE, more cases have significantly suppressed CIN for the heavier precipitating scenes, which is consistent with expectations.

The cases that exhibit statistical significance for CAPE are not always the same for CIN, and vice versa. Table 2 shows a good deal of variability among the cases.

To summarize, in most cases investigated, heavily precipitating areas have significantly higher CAPE and significantly lower CIN. For lightly precipitating regions, the results are more robust for CIN. Namely, there are decreased values of CIN for most areas that are significant, while only 10 out of 24 show significantly increased CAPE. These two general results support the first hypothesis. If CAPE and CIN were independent of the development of heavy precipitation, then we would expect a mean of 1.2 out of 24 cases to be significant. Any count over four would be significant at 95% confidence ($p < 0.05$). The number of cases that reported significant differences is far beyond the expectations of the null hypothesis. Therefore, increases in CAPE and decreases in CIN indicate an increased likelihood of precipitation and, consequently, likely convective initiation.

The same 24 cases and their statistical significance are listed in Table 3 for the t tests examined with respect to the second hypothesis. The terms in Eq. (1) are the same as in the first hypothesis except for one change. Instead of using the CAPE and CIN values at the time and place where precipitation occurs, we extract the CAPE and CIN values from the precipitation

TABLE 3. The same 24 hand-selected cases shown in Table 2 with CAPE and CIN fixed to the 1900 UTC analysis time. MRMS is allowed to vary between 1900 and 0100 UTC as in Table 2. Bold and bold italic fonts are as defined in Table 2.

Case No.	Date	CAPE no precip	CAPE light precip	CAPE heavy precip	CIN no precip	CIN light precip	CIN heavy precip
1	1 Mar	124	**153**	**232**	87	**67**	**45**
2	2 Mar	381	381	**600**	40	61	28
3	3 Mar	61	70	56	68	**51**	**27**
4	12 Mar	313	334	513	74	74	87
5	20 Mar	204	**403**	**427**	142	**55**	**49**
6	24 Mar	208	202	**295**	58	*83*	49
7	27 Mar	732	**870**	893	128	**104**	**77**
8	2 Apr	243	**312**	345	102	**73**	88
9	4 Apr	219	68	—	51	86	—
10	5 Apr	239	**320**	245	34	**17**	10
11	7 Apr	375	265	*217*	93	98	*156*
12	9 Apr	93	**141**	44	262	**132**	**114**
13	13 Apr	178	**267**	—	90	**56**	—
14	22 Apr	310	319	326	35	29	**22**
15	28 Apr	719	**872**	**870**	86	*122*	*103*
16	4 May	699	929	**1105**	142	122	*158*
17	5 May	693	588	*628*	84	*135*	93
18	14 May	670	*544*	*554*	76	82	87
19	16 May	514	*297*	335	36	45	27
20	17 May	521	**946**	**1081**	65	**12**	**11**
21	26 May	579	572	623	49	*59*	*67*
22	14 Jul	360	*234*	*242*	156	162	169
23	19 Jul	644	*570*	612	96	*124*	*164*
24	28 Jul	250	256	218	70	68	*89*

locations but at the satellite overpass time. This one change is equivalent to a current practice of using nearest-neighbor soundings, and any difference between the values in Tables 2 and 3 will therefore represent solely changes due to our trajectory-enhancement procedure. A summary of cases that are consistent with, or are contrary to the hypotheses, are listed in Table 4.

For the nearest-neighbor properties, in lightly precipitating areas 8 out of 24 cases have significantly higher CAPE, and 4 have significantly lower CAPE (bold italics in Table 3), i.e., the opposite of physical expectations. Four of the 12 remaining cases have insignificantly higher CAPE. For areas with heavy precipitation, 7 out of 24 cases have significantly higher CAPE and 4 cases have significantly lower CAPE. The remaining cases are a mix of higher and lower values. The number of cases that exhibit statistical significance in CAPE is less in Table 3 than in Table 2, especially for scenes with heavy precipitation. Furthermore, in the cases where CAPE remains higher and statistically significant in Table 3, in most cases the 1900 UTC CAPE is lower than the trajectory-enhanced

CAPE at the time of precipitation occurrence reported in Table 2.

Concerning CIN, for areas with light precipitation 8 out of 24 cases have significantly lower values of CIN, and 5 cases have significantly higher values of CIN. The remaining insignificant cases are mixed for light precipitation. For areas with heavy precipitation, 7 out of 24 cases have significantly lower values of CIN, and 6 cases have significantly higher values of CIN. The remaining cases are mixed.

For the second hypothesis, nearly as many cases show either statistically significant increases or decreases in CIN for heavy precipitating scenes. This is a much different result than obtained for trajectory-enhanced values in Table 2, where 17 out of 24 cases show significant decreases in CIN, and no cases have significantly higher CIN. A similar trend is observed with CAPE; namely, the number of cases that exhibit statistical significance is in fact smaller for heavy precipitating scenes than light precipitating scenes. These results support the second hypothesis. NUCAPS-FCST CAPE and CIN at the time of convective initiation are far more likely to be in the expected direction than

TABLE 4. The total number of cases that are statistically significant and consistent with the hypotheses vs those that are statistically significant and oppose the hypotheses.

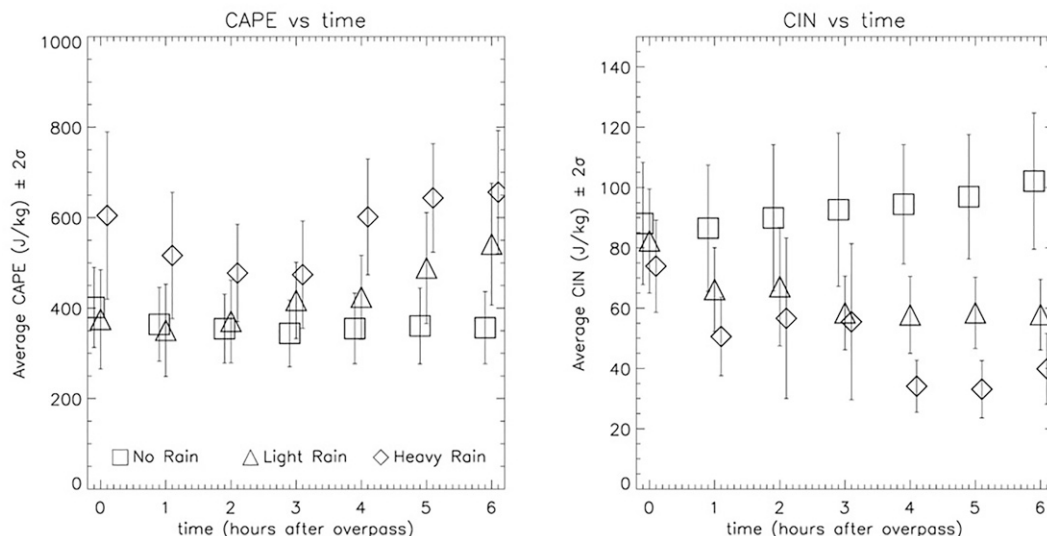|	CAPE light precip	CAPE heavy precip	CIN light precip	CIN heavy precip
Consistent $t = 0$ (Table 3)	9	7	9	7
Oppose $t = 0$ (Table 3)	4	4	5	6
Consistent FCST (Table 2)	11	16	15	17
Oppose FCST (Table 2)	1	0	0	0

FIG. 7. (a) CAPE and (b) CIN for all 24 cases listed in Table 2. Symbols indicate cases with no precipitation (squares), light precipitation (triangles), and heavy precipitation (diamonds). The vertical bars indicate ±2 standard deviation significance.

the retrieved NUCAPS CAPE and CIN at that location during the overpass time. This fact clearly indicates that the trajectory-enhancement procedure correctly identified areas that favor convective development, even if those areas had weaker CAPE or stronger CIN at satellite overpass time.

b. Average over cases by forecast hour

The time-dependent, averaged values of CAPE ($\pm2\sigma$) for nonprecipitating, light, and heavy precipitating scenes derived from Table 2 are shown in Fig. 7a. The largest differences appear at 2100 UTC and afterward with CAPE generally 50–150 J kg^{-1} higher in light precipitating scenes compared to nonprecipitating scenes. Further enhancement is apparent in the heavy precipitating scenes with CAPE generally 100–300 J kg^{-1} higher than nonprecipitating scenes. The time-dependent, averaged values of CIN ($\pm2\sigma$) for nonprecipitating, light, and heavy precipitating scenes derived from Table 2 are shown in Fig. 7b. As with CAPE, the largest differences appear at 2000 UTC and afterward with CIN generally 10–40 J kg^{-1} lower in light precipitating scenes compared to nonprecipitating scenes. Further enhancement is apparent in the heavy precipitating scenes with CIN generally 20–60 J kg^{-1} lower than nonprecipitating scenes.

To summarize, scenes that eventually produce convective precipitation contain higher values of CAPE in the latter periods of NUCAPS-FCST, usually from 2100 UTC onward, and lower values of CIN in the latter periods of NUCAPS-FCST, typically from 2000 UTC onward.

c. Average over all cases and forecast hours

The above results considered the frequency with which precipitation coincided with estimated enhancement of CAPE or suppression of CIN. In Fig. 8, we consider the mean CAPE and CIN values ($\pm2\sigma$) calculated across the 21 case-mean

properties from Tables 2 and 3 that contain values for light and heavy precipitation. First, Fig. 8 shows that progressively heavier precipitation coincides with increased mean CAPE and decreased mean CIN. The stronger gradients in the black relative to the gray values represent the improvement from trajectory enhancement compared to the nearest-neighbor overpass values. This is particularly notable for CIN: advection clearly causes development of areas of low CIN prior to convection onset. There are negligible differences at overpass time but NUCAPS-FCST shows an approximate halving of mean CIN for heavy-precipitation areas compared with no-precipitation areas. Despite the tendencies in Fig. 8, the differences between the mean CAPE or CIN across all cases are not significant between any of the precipitation classifications.

However, it is not necessarily the absolute value of CAPE or CIN that defines whether precipitation is likely to occur. Convection triggers in all of these cases, and our hypothesis is that it is more likely to occur in areas of relatively higher CAPE and/or lower CIN, compared with the average properties of that day. The analysis of Tables 2 and 3 reported on significant differences in CAPE or CIN within each individual case. The analogous mean comparisons are shown in Fig. 8. For these panels, the no-precipitation CAPE or CIN was subtracted from the light- or heavy-precipitation value on the same day, generating 21 estimates of CAPE or CIN enhancement or suppression relative to average conditions. In this case, using the NUCAPS overpass values suggest insignificantly enhanced CAPE in precipitating areas. Meanwhile NUCAPS-FCST trajectory-enhanced CAPE and CIN show significant differences from no precipitation areas for all precipitation classifications, and show stronger deviations for heavy rather than light precipitation. The differences between light and heavy precipitation areas are not significant at the
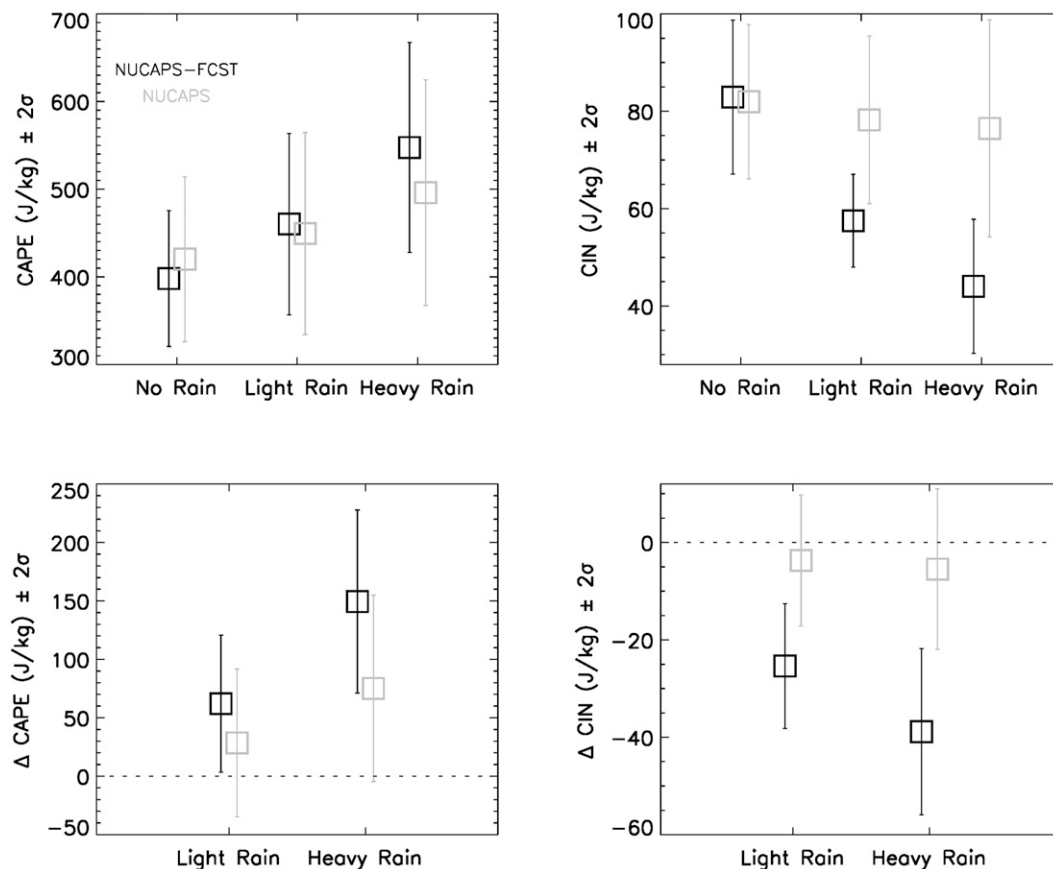
FIG. 8. (top) Mean $\pm 2\sigma$ of case CAPE and CIN. Each point is the mean of the 21 cases for which CAPE and CIN are available on both Tables 2 and 3 for all precipitation amounts. (bottom) Mean $\pm 2\sigma$ for the change in CAPE and CIN values relative to no precipitation. For each case the light rain minus no rain or heavy rain minus no rain values are calculated, and then the mean of these 21 values is plotted. Black values are the trajectory-enhanced NUCAPS-FCST results from Table 2, and gray values are the satellite overpass time results from Table 3. The horizontal dotted lines denote the zero CAPE and CIN change lines and help depict the statistical significance of NUCAPS-FCST compared to NUCAPS.

2σ level, but trend in the direction we expect from our hypothesis.

Taken together, this evidence allows one to conclude that there is added value in trajectory-enhanced CAPE and CIN calculations at the times following the satellite overpass. Simple advection of LEO snapshots forward in time exhibits skill in determining where likely convection eventually initiates, providing a nowcasting methodology for using operational satellite thermodynamic soundings.

6. Discussion and summary

We have described and evaluated a novel nowcasting methodology that extends snapshots of low-Earth-orbiting (LEO) soundings up to 6 h into the future using NUCAPS sounding retrievals from the *Suomi NPP* and *NOAA-20* satellite platforms. As an extension of Kalmus et al. (2019), this nowcasting methodology applied to NUCAPS soundings is termed "NUCAPS-Forecast" (NUCAPS-FCST), and has been made available within Advanced Weather Interactive Processing

Systems Evolution Project (AWIPS II) for experimental use in a quasi-operational weather forecasting environment. The methodology uses parcel forward-trajectory calculations with the NOAA's HYSPLIT model and GFS winds to recreate future soundings of temperature (T) and specific humidity (q) at regularly gridded intervals after the satellite observing time. Calculations of CAPE and CIN are made with SHARPpy and are evaluated against gridded, hourly accumulated rainfall obtained from MRMS observations for 24 hand-selected cases over CONUS. Until an advanced geostationary hyperspectral IR sounder is deployed to monitor the CONUS and surrounding regions, this method can be used to fill in temporal gaps.

Two hypotheses are tested that relate to the time and space information provided by NUCAPS-FCST CAPE and CIN to proximity MRMS QPE. The first is that *increased values of CAPE, and decreased values of CIN over scales of a few hundred kilometers or less, indicate increased likelihood of convective initiation*. The second is that *CAPE and CIN analyses at 1900 UTC are less likely to predict convective initiation after*

1900 UTC than CAPE and CIN fields estimated at later times resulting from the HYSPLIT forward trajectories. Using a two-sided *t* test, statistically significant increases in CAPE and decreases in CIN are found for precipitating scenes compared to nonprecipitating scenes for most of the cases examined. The statistical significance is stronger for areas with heavy precipitation compared to light precipitation. Furthermore, the statistical significance for CAPE and CIN between precipitating scenes compared to nonprecipitating scenes is only enhanced as time increases past 1900 UTC. These results suggest that a simplified approach of adiabatic parcel advection of LEO satellite sounding snapshots forward in time can identify locations and times where convective initiation is more likely.

There are some important caveats to this investigation. First, cases that included convective initiation were selected, so results are based on the conditions in which we expect the best performance of NUCAPS-FCST and do not necessarily apply to ongoing convection, or convective systems that initiated before the overpass time. However, we note that the peak in severe convective event occurrence using the NCEI Storm Events database is several hours after the 1330 LT overpass (Kalmus et al. 2019). Second, we only examined averages and standard errors of CAPE and CIN given the occurrence of precipitation (or the lack thereof), rather than examine averages and standard errors of precipitation (or the lack thereof) in a range of CAPE and CIN bins. Only small geographical areas have actively precipitating convection at any given time, even for values of CAPE and CIN that are favorable for convective initiation. Third, only the mean values of *light* and *heavy* precipitation were investigated, which are averaged over 0.5° × 0.5° areal grid boxes. This investigation did not consider the area coverage or precipitation intensity at the native grid resolution of MRMS at 0.01° × 0.01°.

A distinction between a "quasi-operational" version and a "research quality" version of NUCAPS-FCST should be made. In this study, a "quasi-operational" version of NUCAPS-FCST is described and evaluated which adheres to requirements on production, latency, and delivery to the HWT. The algorithm is optimized for rapid processing using parallelized code and NUCAPS files from direct broadcast data streams. Because of the need for rapid turnaround for use in AWIPS II, surface observations that do not yet exist (i.e., in the future) cannot be used to correct for the surface and boundary layer structure that is important for improving estimates of CAPE and CIN (Gartzke et al. 2017). A promising approach combines NUCAPS soundings with Meteorological Assimilation Data Ingest System (MADIS) surface observations, which are made available with subhourly time latency for seamless convective parameter calculations (Bloch et al. 2019). Another promising technique combines NUCAPS soundings, ABI observations, and model analyses using a deep neural network (Ma et al. 2021). These techniques, unfortunately, cannot be applied because of the aforementioned latency requirements. Using surface observations would be ideal in a "research quality" version of NUCAPS-FCST that is not constrained by latency requirements.

NWP forecast fields of T and T_d could meet the latency requirements to improve surface and boundary layer structure for quasi-operational nowcasting. However, this type of data fusion approach requires significant research effort as model biases will impact NUCAPS-FCST. Spatial and temporal mismatches between NWP forecasted and observed convection will lead to mismatches and discontinuities in NWP and NUCAPS-FCST observations of thermodynamic structure in the boundary layer.

APPENDIX A

Description of Real-Time NUCAPS-FCST Method

A strategy was developed to accelerate the methodology using parallelization, and to customize data delivery, ingest and display within the AWIPS II operational decision support system. The SPoRT team downloaded and processed low-latency NUCAPS Environmental Data Records (EDRs) from multiple direct broadcast sites at the University of Wisconsin/Space

Science and Engineering Center (UW/SSEC). Data were supplemented from the University of Miami and the Naval Research Laboratory in Monterey, California, during spring/summer 2020 to provide improved coverage of environmental conditions at low latitudes (especially over the Gulf of Mexico) and the western United States, respectively.

The parallelization of HYSPLIT to generate forward trajectories from the NUCAPS initial T and q profiles was handled by assigning each NUCAPS granule file production to an individual processor on the SPoRT computing cluster. Each NUCAPS granule file contains 120 soundings, thereby resulting in 120 HYSPLIT output trajectory files with 0–6-h forward-trajectories in hourly intervals. The number of NUCAPS granule files changed from day to day and among the different initialization times due to varying *Suomi NPP* and *NOAA-20* swath coverage across the predefined CONUS domain (23°–52°N and 127°–64.5°W). The number of processors invoked were adapted to the number of input granule files. Additional parallelization was implemented in the gridding of stability indices from the merged soundings processed through the SHARPpy package at each $0.5° \times 0.5°$ grid box. The longitude dimension was evenly divided among 25 processors for computing CAPE, CIN, LCL, LFC, and equilibrium level (EL) that is output into a gridded netcdf file.

Additional postprocessing of the gridded netcdf file was done to convert the output to gridded binary-version 2 (GRIB2) format for decoding and displaying within AWIPS II. The five convective indices were encoded into unique, available parameter numbers within an existing GRIB2 decoder table interpreted by AWIPS II. We then coordinated with personnel at HWT, providing them with the decoding table and instructions for ingesting and displaying the data in their AWIPS II workstations. The GRIB2 files were transmitted in real time to HWT via the Local Data Manager software and fed into AWIPS II with less than 2-h latency. Due to an anomaly with *Suomi NPP* prior to the HWT in spring 2019, only NUCAPS soundings from *NOAA-20* were used to generate gridded NUCAPS-FCST output for analysis by participants of the HWT. In spring 2020, NUCAPS soundings from both the *Suomi NPP* and *NOAA-20* satellites were included. This increased the computational workload and thus required some code modifications and run-time adjustments, but resulted in occasional near CONUS-wide coverage.

Finally, SPoRT also developed an internal project web page for displaying real-time and archived output of all convective indices for every initialization date and time of each day during 2019 and 2020. Both daytime and nighttime NUCAPS soundings were utilized to generate 0–6-h forecast output in five separate streams initialized daily at 0700 and 0900 UTC (nighttime), and 1700, 1900, and 2100 UTC (daytime), driven by GFS model forecast files formatted for HYSPLIT runs as acquired from the Air Resources Laboratory (ARL) ftp server.

APPENDIX B

Intercomparison of NUCAPS-FCST and Radiosonde Soundings

A quantitative estimate of the performance of NUCAPS-FCST derived T and q against a large set of radiosondes warrants a thorough study but is beyond the scope of this investigation. To perform spot checks for NUCAPS-FCST in proximity to 0000 UTC, comparisons were made against available Atmospheric Radiation Measurement (ARM) program dedicated radiosonde launches at the Lamont, Oklahoma, station at the Southern Great Plains (SGP) ARM site. A total of 16 matches were found for the 24 case studies.

A total of 3 of 16 comparisons are shown in Fig. B1 that represent a typical case (24 March 2020), a perceived "degradation" of NUCAPS-FCST compared to NUCAPS (27 March 2020), and a perceived "improvement" of NUCAPS-FCST compared to NUCAPS (14 May 2020). For the 24 March 2020 case, both NUCAPS and NUCAPS-FCST capture changes in the T lapse rate and appear to also capture the vertical structure of q in the lower and middle troposphere. For the 27 March 2020 case, the T for NUCAPS-FCST is cooler than NUCAPS and the radiosonde and also shows excessive moistening between 700 and 900 hPa compared to the radiosonde. For the 14 May 2020 case, NUCAPS-FCST better captures T between 950 and 700 hPa compared to NUCAPS and, furthermore, shows a somewhat closer match of q to the radiosonde for much of the troposphere.

These initial comparisons against radiosondes serve as a useful sanity check for the performance of NUCAPS-FCST. With a much larger set of radiosondes over a longer period of time, in different seasons, within different meteorological regimes, across a range of latitudes and longitudes, and for a range of sampling variations (e.g., Fig. 1), a more robust set of quantitative performance metrics can be determined.
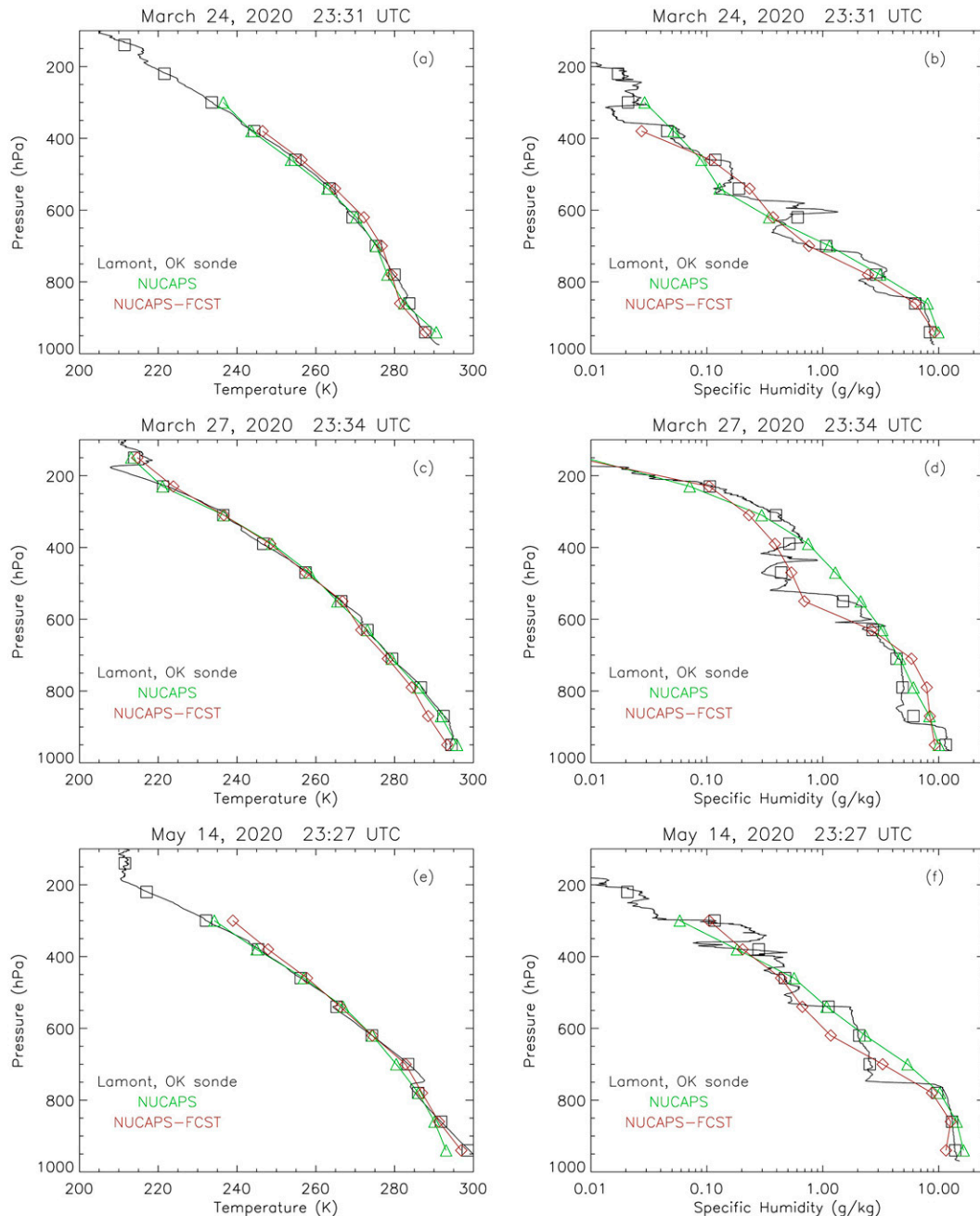
FIG. B1. Three Lamont, OK, radiosondes at full vertical resolution (solid black line), smoothed to 80-hPa layers used in NUCAPS-FCST (black squares), compared against NUCAPS (red line and diamonds), and NUCAPS-FCST (green line and triangles). The NUCAPS and NUCAPS-FCST T and q are time interpolated in between 2300 and 0000 UTC to the radiosonde times listed in the figure titles. The spatial collocations are nearest neighbors based on the mean latitude and longitude for each radiosonde, which may significantly vary depending on wind direction and speed.

REFERENCES

Adkins, J., and Coauthors, 2021: Geostationary Extended Observations (GeoXO) hyperspectral infrared sounder value assessment report. NOAA/NESDIS Tech. Rep., 103 pp., https://repository.library.noaa.gov/view/noaa/32921.

Barnet, C. D., and Coauthors, 2021: NOAA Unique Combined Atmospheric Processing System (NUCAPS). Algorithm Theoretical Basis Doc., version 3.1, 115 pp., https://www.star.nesdis. noaa.gov/jpss/documents/ATBD/ATBD_NUCAPS_v3.1.pdf.

Berndt, E. B., B. T. Zavodsky, and M. J. Folmer, 2016: Development and application of atmospheric infrared sounder ozone

retrieval products for operational meteorology. *IEEE Trans. Geosci. Remote Sens.*, **54**, 958–967, https://doi.org/10.1109/TGRS.2015.2471259.

——, and Coauthors, 2020: Gridded satellite sounding retrievals in operational weather forecasting: Product description and emerging applications. *Remote Sens.*, **12**, 3311, https://doi.org/10.3390/rs12203311.

Bloch, C., R. O. Knuteson, A. Gambacorta, N. R. Nalli, J. Gartzke, and L. Zhou, 2019: Near-real-time surface-based CAPE from merged hyperspectral IR satellite sounder and surface meteorological station data. *J. Appl. Meteor. Climatol.*, **58**, 1613–1632, https://doi.org/10.1175/JAMC-D-18-0155.1.

Blumberg, W. G., K. T. Halbert, T. A. Supinie, P. T. Marsh, R. L. Thompson, and J. A. Hart, 2017: SHARPpy: An open-source sounding analysis toolkit for the atmospheric sciences. *Bull. Amer. Meteor. Soc.*, **98**, 1625–1636, https://doi.org/10.1175/BAMS-D-15-00309.1.

Blumstein, D., and Coauthors, 2004: IASI instrument: Technical overview and measured performances. *Proc. SPIE*, **5543**, 196–207, https://doi.org/10.1117/12.560907.

Botes, D., J. R. Mecikalski, and G. J. Jedlovec, 2012: Atmospheric Infrared Sounder (AIRS) sounding evaluation and analysis of the pre-convective environment. *J. Geophys. Res.*, **117**, D09205, https://doi.org/10.1029/2011JD016996.

Burrows, C., 2019: Assimilation of radiance observations from geostationary satellites: Second year report. ECMWF/EUMETSAT Tech. Rep. 51, 50 pp., https://www.ecmwf.int/node/19233.

Calhoun, K. M., K. L. Berry, D. M. Kingfield, T. Meyer, M. J. Krocak, T. M. Smith, G. Stumpf, and A. Gerard, 2021: The experimental warning program of NOAA's Hazardous Weather Testbed. *Bull. Amer. Meteor. Soc.*, **120**, E2229–E2246, https://doi.org/10.1175/BAMS-D-21-0017.1.

Chahine, M. T., and Coauthors, 2006: AIRS: Improving weather forecasting and providing new data on greenhouse gases. *Bull. Amer. Meteor. Soc.*, **87**, 911–926, https://doi.org/10.1175/BAMS-87-7-911.

Divakarla, M. G., C. D. Barnet, M. D. Goldberg, L. M. McMillin, E. Maddy, W. Wolf, L. Zhou, and X. Liu, 2006: Validation of atmospheric infrared sounder temperature and water vapor retrievals with matched radiosonde measurements and forecasts. *J. Geophys. Res.*, **111**, D09S15, https://doi.org/10.1029/2005JD006116.

Doswell, C. A., III, and J. S. Evans, 2003: Proximity sounding analysis for derechos and supercells: An assessment of similarities and differences. *Atmos. Res.*, **67–68**, 117–133, https://doi.org/10.1016/S0169-8095(03)00047-4.

Esmaili, R. B., and Coauthors, 2020: Adapting satellite soundings for operational forecasting within the Hazardous Weather Testbed. *Remote Sens.*, **12**, 886, https://doi.org/10.3390/rs12050886.

Feltz, W. F., and J. R. Mecikalski, 2002: Monitoring high-temporal-resolution convective stability indices using the ground-based Atmospheric Emitted Radiance Interferometer (AERI) during the 3 May 1999 Oklahoma–Kansas tornado outbreak. *Wea. Forecasting*, **17**, 445–455, https://doi.org/10.1175/1520-0434(2002)017<0445:MHTRCS>2.0.CO;2.

Gartzke, J., R. Knuteson, G. Przybyl, S. Ackerman, and H. Revercomb, 2017: Comparison of satellite-, model-, and radiosonde-derived convective available potential energy in the Southern Great Plains region. *J. Appl. Meteor. Climatol.*, **56**, 1499–1513, https://doi.org/10.1175/JAMC-D-16-0267.1.

Gravelle, C. M., J. R. Mecikalski, W. E. Line, K. M. Bedka, R. A. Petersen, J. M. Sieglaff, G. T. Stano, and S. J. Goodman, 2016: Demonstration of a GOES-R satellite convective

toolkit to "bridge the gap" between severe weather watches and warnings: An example from the 20 May 2013 Moore, Oklahoma, tornado outbreak. *Bull. Amer. Meteor. Soc.*, **97**, 69–84, https://doi.org/10.1175/BAMS-D-14-00054.1.

Han, Y., and Coauthors, 2013: Suomi NPP CrIS measurements, sensor data record algorithm, calibration and validation activities, and record data quality. *J. Geophys. Res. Atmos.*, **118**, 12 734–12 748, https://doi.org/10.1002/2013JD020344.

Hoffman, R. N., and R. Atlas, 2016: Future observing system simulation experiments. *Bull. Amer. Meteor. Soc.*, **97**, 1601–1616, https://doi.org/10.1175/BAMS-D-15-00200.1.

Holmlund, K., and Coauthors, 2021: Meteosat Third Generation (MTG): Continuation and innovation of observations from geostationary orbit. *Bull. Amer. Meteor. Soc.*, **102**, E990–E1015, https://doi.org/10.1175/BAMS-D-19-0304.1.

Iturbide-Sanchez, F., S. R. S. da Silva, Q. Liu, K. L. Pryor, M. E. Pettey, and N. R. Nalli, 2018: Toward the operational weather forecasting application of atmospheric stability products derived from NUCAPS CrIS/ATMS soundings. *IEEE Trans. Geosci. Remote Sens.*, **56**, 4522–4545, https://doi.org/10.1109/TGRS.2018.2824829.

Jedlovec, G. J., 2013: Transitioning research satellite data to the operational weather community: The SPoRT paradigm [Organization Profiles]. *IEEE Geosci. Remote Sens. Mag.*, **1**, 62–66, https://doi.org/ 10.1109/MGRS.2013.2244704.

Jones, T. A., and D. J. Stensrud, 2012: Assimilating AIRS temperature and mixing ratio profiles using an ensemble Kalman filter approach for convective-scale forecasts. *Wea. Forecasting*, **27**, 541–564, https://doi.org/10.1175/WAF-D-11-00090.1.

Kalluri, S., and Coauthors, 2022: Validation and utility of satellite retrievals of atmospheric profiles in detecting and monitoring significant weather events. *Bull. Amer. Meteor. Soc.*, **103**, E570–E590, https://doi.org/10.1175/BAMS-D-20-0126.1.

Kalmus, P., B. H. Kahn, S. W. Freeman, and S. C. van den Heever, 2019: Trajectory-enhanced AIRS observations of environmental factors driving severe convective storms. *Mon. Wea. Rev.*, **147**, 1633–1653, https://doi.org/10.1175/MWR-D-18-0055.1.

Li, Z., and Coauthors, 2018: Value-added impact of geostationary hyperspectral infrared sounders on local severe storm forecasts—Via a quick regional OSSE. *Adv. Atmos. Sci.*, **35**, 1217–1230, https://doi.org/10.1007/s00376-018-8036-3.

Ma, Z., Z. Li, J. Li, T. J. Schmit, L. Cucurull, R. Atlas, and B. Sun, 2021: Enhance low level temperature and moisture profiles through combining NUCAPS, ABI observations, and RTMA analysis. *Earth Space Sci.*, **8**, e2020EA001402, https://doi.org/10.1029/2020EA001402.

Maddy, E. S., and C. D. Barnet, 2008: Vertical resolution estimates in version 5 of AIRS operational retrievals. *IEEE Trans. Geosci. Remote Sens.*, **46**, 2375–2384, https://doi.org/10.1109/TGRS.2008.917498.

Nalli, N. R., and Coauthors, 2013: Validation of satellite sounder environmental data records: Application to the cross-track infrared microwave sounder suite. *J. Geophys. Res. Atmos.*, **118**, 13 628–13 643, https://doi.org/10.1002/2013JD020436.

——, and Coauthors, 2018: Validation of atmospheric profile retrievals from the SNPP NOAA-unique combined atmospheric processing system. Part 1: Temperature and moisture. *IEEE Trans. Geosci. Remote Sens.*, **56**, 180–190, https://doi.org/10.1109/TGRS.2017.2744558.

Parker, M. D., 2014: Composite VORTEX2 supercell environments from near-storm soundings. *Mon. Wea. Rev.*, **142**, 508–529, https://doi.org/10.1175/MWR-D-13-00167.1.

Petersen, R. A., and R. M. Aune, 2007: An objective nowcasting tool that optimizes the impact of satellite derived sounder products in very-short-range forecasts. *11th Symp. on Integrated Observing and Assimilation Systems for the Atmosphere, Oceans, and Land Surface (IOAS-AOLS)*, San Antonio, TX, Amer. Meteor. Soc., 3.17, https://ams.confex.com/ams/pdfpapers/117341.pdf.

Rasmussen, E. N., and D. O. Blanchard, 1998: A baseline climatology of sounding-derived supercell and tornado forecast parameters. *Wea. Forecasting*, **13**, 1148–1164, https://doi.org/10.1175/1520-0434(1998)013<1148:ABCOSD>2.0.CO;2.

Schmit, T. J., J. Li, S. A. Ackerman, and J. J. Gurka, 2009: High-spectral- and high-temporal-resolution infrared measurements from geostationary orbit. *J. Atmos. Oceanic Technol.*, **26**, 2273–2292, https://doi.org/10.1175/2009JTECHA1248.1.

Smith, N., and C. D. Barnet, 2020: CLIMCAPS observing capability for temperature, moisture, and trace gases from AIRS/AMSU and CrIS/ATMS. *Atmos. Meas. Tech.*, **13**, 4437–4459, https://doi.org/10.5194/amt-13-4437-2020.

Smith, W. L., Q. Zhang, M. Shao, and E. Weisz, 2020: Improved severe weather forecasts using LEO and GEO satellite soundings. *J. Atmos. Oceanic Technol.*, **37**, 1203–1218, https://doi.org/10.1175/JTECH-D-19-0158.1.

Stein, A. F., R. R. Draxler, G. D. Rolph, B. J. B. Stunder, M. D. Cohen, and F. Ngan, 2015: NOAA's HYSPLIT atmospheric transport and dispersion modeling system. *Bull. Amer. Meteor. Soc.*, **96**, 2059–2077, https://doi.org/10.1175/BAMS-D-14-00110.1.

Sun, B., A. Reale, F. H. Tilley, M. E. Pettey, N. R. Nalli, and C. D. Barnet, 2017: Assessment of NUCAPS S-NPP CrIS/ATMS sounding products using reference and conventional radiosonde observations. *IEEE J. Sel. Top. Appl. Earth Obs. Remote Sens.*, **10**, 2499–2509, https://doi.org/10.1109/JSTARS.2017.2670504.

Thompson, R. L., R. Edwards, J. A. Hart, K. L. Elmore, and P. Markowski, 2003: Close proximity soundings within supercell environments obtained from the Rapid Update Cycle. *Wea. Forecasting*, **18**, 1243–1261, https://doi.org/10.1175/1520-0434(2003)018<1243:CPSWSE>2.0.CO;2.

Tobin, D. C., and Coauthors, 2006: Atmospheric radiation measurement site atmospheric state best estimates for atmospheric infrared sounder temperature and water vapor retrieval validation. *J. Geophys. Res.*, **111**, D09S14, https://doi.org/10.1029/2005JD006103.

Wagner, T. J., W. F. Feltz, and S. A. Ackernam, 2008: The temporal evolution of convective indices in storm-producing environments. *Wea. Forecasting*, **23**, 786–794, https://doi.org/10.1175/2008WAF2007046.1.

Wang, P., Z. Li, J. Li, and T. J. Schmit, 2021: Added-value of GEO-hyperspectral infrared radiances for local severe storm forecasts using the hybrid OSSE method. *Adv. Atmos. Sci.*, **38**, 1315–1333, https://doi.org/10.1007/s00376-021-0443-1.

Wang, X., D. Parrish, D. Kleist, and J. Whitaker, 2013: GSI 3DVar-based ensemble–variational hybrid data assimilation for NCEP global forecast system: Single-resolution experiments. *Mon. Wea. Rev.*, **141**, 4098–4117, https://doi.org/10.1175/MWR-D-12-00141.1.

Weaver, G. M., N. Smith, E. B. Berndt, K. D. White, J. F. Dostalek, and B. T. Zavodsky, 2019: Addressing the cold air aloft aviation challenge with satellite sounding observations. *J. Oper. Meteor.*, **7**, 138–152, https://doi.org/10.15191/nwajom.2019.0710.

Weisz, E., and W. P. Menzel, 2019: Imager and sounder data fusion to generate sounder retrieval products at an improved spatial and temporal resolution. *J. Appl. Remote Sens.*, **13**, 034506, https://doi.org/10.1117/1.JRS.13.034506.

——, N. Smith, and W. L. Smith Sr., 2015: The use of hyperspectral sounding information to monitor atmospheric tendencies leading to severe local storms. *Earth Space Sci.*, **2**, 369–377, https://doi.org/10.1002/2015EA000122.

WMO, 2017: Guidelines for nowcasting techniques. WMO Tech. Rep. 1198, 82 pp., https://library.wmo.int/doc_num.php?explnum_id=3795.

Wong, S., E. J. Fetzer, M. Schreier, G. Manipon, E. F. Fishbein, B. H. Kahn, Q. Yue, and F. W. Irion, 2015: Cloud-induced uncertainties in AIRS and ECMWF temperature and specific humidity. *J. Geophys. Res. Atmos.*, **120**, 1880–1901, https://doi.org/10.1002/2014JD022440.

Yang, J., Z. Zhang, C. Wei, F. Lu, and Q. Guo, 2017: Introducing the new generation of Chinese geostationary weather satellites, Fengyun-4. *Bull. Amer. Meteor. Soc.*, **98**, 1637–1658, https://doi.org/10.1175/BAMS-D-16-0065.1.

Yin, R., W. Han, Z. Gao, and J. Li, 2021: Impact of high temporal resolution FY-4A Geostationary Interferometric Infrared Sounder (GIIRS) radiance measurements on typhoon forecasts: Maria (2018) case with GRAPES global 4D-Var assimilation system. *Geophys. Res. Lett.*, **48**, e2021GL093672, https://doi.org/10.1029/2021GL093672.

——, ——, H. Wang, and J. Wang, 2022: Impacts of FY-4A GIIRS water vapor channels data assimilation on the forecast of "21.7" extreme rainstorm in Henan, China with CMA-MESO. *Remote Sens.*, **14**, 5710, https://doi.org/10.3390/rs14225710.

Zhang, J., and Coauthors, 2016: Multi-Radar Multi-Sensor (MRMS) quantitative precipitation estimation: Initial operating capabilities. *Bull. Amer. Meteor. Soc.*, **97**, 621–638, https://doi.org/10.1175/BAMS-D-14-00174.1.